

NONLINEAR BENDING COMPLIANCE OF CLOSED-SECTIONED COMPOSITE BEAM STRUCTURES BY LOCAL COMPRESSION FLANGE BUCKLING

F. Schadt^{*1}, M. Rueppel¹, C. Brauner¹, K. Masania², C. Dransfeld¹, T. Ricard³

¹Institute of Polymer Engineering, FHNW University of Applied Sciences and Arts Northwestern Switzerland, Klosterzelgstrasse 2, CH-5210 Windisch, Switzerland

*Email: fabian.schadt@fhnw.ch

²Complex Materials, Department of Materials, ETH Zürich, 8093 Zürich, Switzerland

³North Thin Ply Technology Sàrl, Chemin du Closel 3, CH-1020 Renens, Switzerland

Web Page: <https://www.thinplytechnology.com>

Keywords: Shape adaptation, Nonlinear compliance, Buckling, Postbuckling, Thin ply composite

Abstract

Passive spanwise bending shape-adaption has the potential to increase the efficiency and manoeuvrability of vehicles with wing-like structures. This paper presents a passive spanwise bending shape-adaption concept for highly loaded wing-like structures based on local buckling of the compression flange at a prescribed external bending moment. Buckling reduces the in-plane stiffness of the compression flange and thus yields a beam design with a high prebuckling and a low postbuckling bending stiffness. The investigated concept is experimentally validated using a composite four-point bending beam, which is designed to experience compression flange buckling between the load introductions. The point of buckling is at 374.80 Nm, and ultimate failure occurred in the experiment at 524 Nm, which results in a postbuckling range of 149.2 Nm. The bending stiffness was reduced by more than 41% after the point of buckling which shows the effectiveness of compression flange buckling for nonlinear bending compliance. This proof of concept has demonstrated for the first time, that compression flange buckling is a viable structural concept for highly loaded composite beam structures to achieve nonlinear bending compliance.

1. Introduction

Compliant mechanisms exploit elastic deformations in materials and structures to provide a large degree of structural deformability without the need for conventional pin-jointed mechanisms, which offers advantages such as increased wear resistance, fewer assembly steps and improved strength-to-weight ratios. Compliant mechanisms are of increasing importance for lightweight, shape-adaptable structural applications [1] such as aircraft structures. Wing-like structures with shape-adaptability have the potential to improve performance and efficiency over conventional wing designs [2] through e.g. spanwise bending shape-adaption of wing spars, reducing drag and increasing manoeuvrability [3]. The aim of this work was to develop and test a highly loaded wing spar structure with a nonlinear bending compliance. This compliance is generated by local elastic compression flange buckling in the wing spar at a prescribed external bending moment. Buckling in the compression flange leads to an in-plane stiffness reduction in the flange and thus yields a beam design with a high prebuckling and a low postbuckling bending stiffness.

The investigated concept was verified on a four-point bending beam, which is designed to experience compression flange buckling between the load introductions. The constraints for the four-point bending beam geometry and the expected load range were derived from the dimensions of a generic A-Class catamaran hydrofoil.

2. Beam Models

An analytical beam model was developed as a first approximation of the initial beam bending stiffness, the beam displacement, and the bending moment at the point of buckling. The analytical four-point bending beam model is based on the Euler-Bernoulli beam model for which the stiffness properties are calculated with the classical laminate theory [4]. The four-point bending beam cross section was modelled with top, bottom, and shear web laminates (Fig. 1, Cross section). The span of the beam was divided into three sections (Fig. 1, Side view), each with a separate set of top, bottom, and shear web laminates.

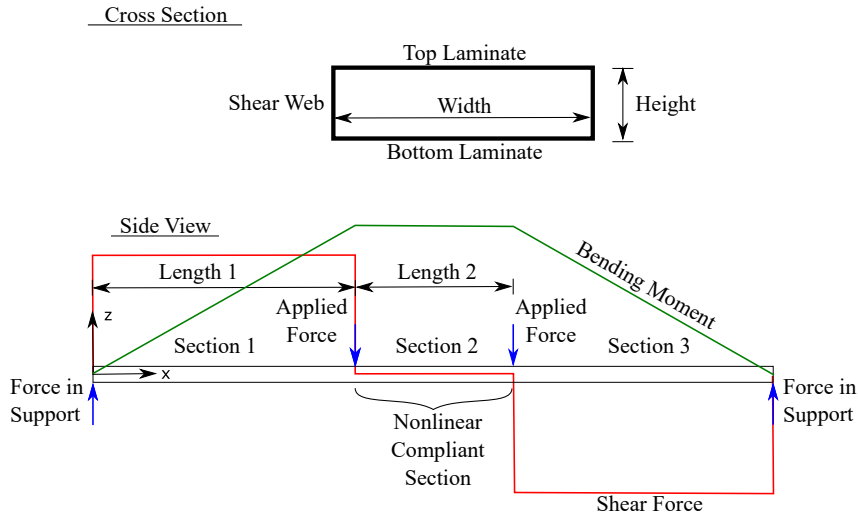


Figure 1. Top: Cross section of the analytical four-point bending beam model; Bottom: Free body diagram of the four point-bending beam.

The critical buckling load was calculated by treating the top laminate of section 2 (Fig. 1 Side view) as a long plate with fully constraint unloaded edges parallel to the beam and simply supported loaded edges across the beam. The critical buckling load of such a constraint plate is [5]:

$$N_{xcr} = \frac{\pi^2}{b^2} \left(D_{11} \frac{b^2}{l_x^2} + 5.139 D_{22} \frac{l_x^2}{b^2} + 2.62(D_{12} + 2D_{66}) \right) \quad (1)$$

Where N_{xcr} is the critical in-plane force per unit width at which the plate buckles, D_{ij} are the bending stiffness matrix components, b is the plate width, and l_x is the buckling half-wave length. The buckling plate dimensions were defined by the length of section 2 (Fig. 1 Side view) and the effective buckling field width. The effective buckling field width is calculated by subtracting the corner radii of the beam cross section from the width of the top laminate.

Equation (1) is only valid for special orthotropic laminates ($D_{13} = D_{23} = 0$) [5]. Despite a possible overestimation in critical buckling load for fully constrained laminates which are non-special orthotropic ($D_{13} = D_{23} \neq 0$) [6] Equation (1) was used for a quasi-isotropic laminate in absence of a suitable closed formed expression.

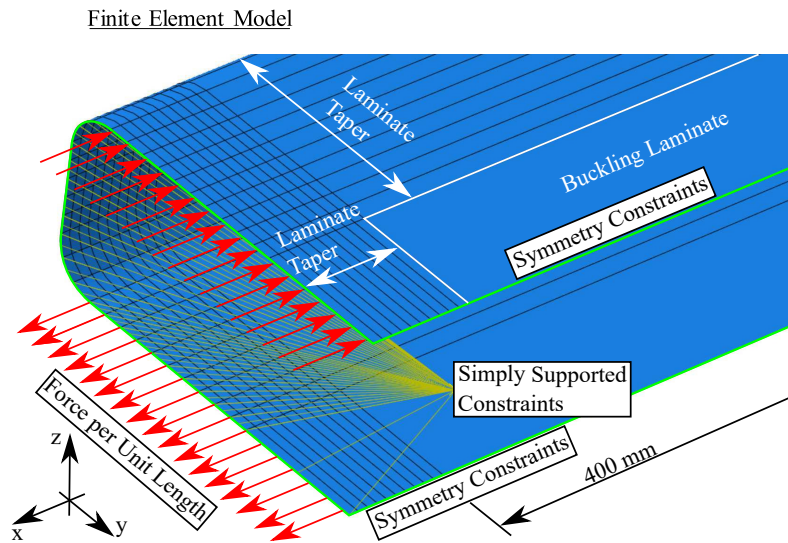


Figure 2. Derived finite element model of beam section 2 without mesh, showing the transition of section 1 to section 2 of the four-point bending beam.

A finite element model was created in ABAQUS[®] Standard/FEA [7] and comprised only the nonlinear compliant section of the four-point bending beam (section 2 in Fig. 1). The model was partitioned in the area of the laminate tapers for modelling all ply drop-offs in the beam section (Fig. 2). The ends of the nonlinear compliant beam section were connected to reference nodes placed in the cross section centre of the beam section at the ends of the buckling laminate. The beam section was simply supported at the reference nodes and the long edges of the half beam section were constraint by symmetry constraints. The difference in fibre modulus between tension and compression (Tab. 1) was accounted for by modelling the beam section above the neutral axis with compressive material properties, and the laminate in the tension side of the beam section below the neutral axis with tensile material properties. The finite element model was meshed with quadratic shell elements (S8R), 0.53×0.53 mm in size for the top laminate and the adjacent radii, and 0.53×1.6 mm in size for the shear webs and the bottom laminate. The resulting accuracy with these element sizes was checked in a mesh convergence study. The composite beam section was analysed using the modified Riks method.

3. Beam Design and Material

The outer beam dimensions were selected such that the beam resembles a spar of a wing structure with a chord length of 0.194 m. The outside beam dimensions (Fig. 3), are 1.2 m in length, 0.60 m in width and 0.15 m in height. The radius of all four edges is 3.5 mm. The buckling field is 0.40 m long, which yields a length to width ratio of approximately 7.55.

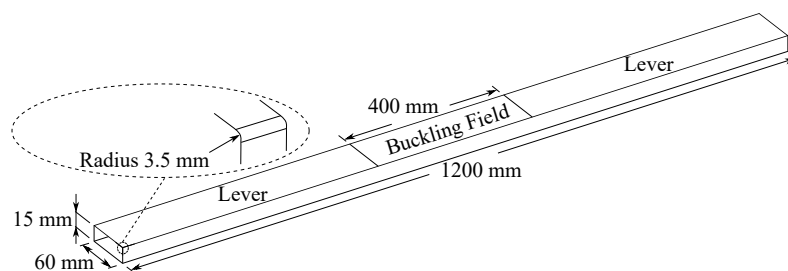


Figure 3. Four-point bending beam dimensions.

The four-point bending beam was manufactured with a top laminate and a bottom laminate, which were bonded together in a successive manufacturing step. The top laminate was designed as a U-shape to ensure precise manufacturing of the ply drop-offs and buckling field (Fig. 4). The bottom laminate was designed as a C-shape, which provided a good stiffness transition in the area of the buckling field and increased the bond area.

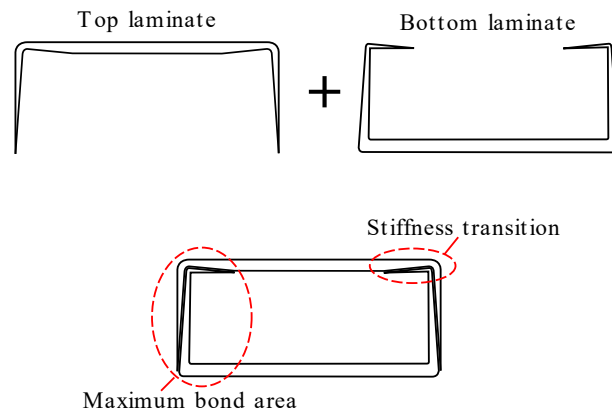


Figure 4. Laminate design concept.

The laminate layup was selected to comprise fibre angles of 0° , $\pm 45^\circ$ and 90° , enabling a fibre angle change between each ply of 45° . However, preliminary design iterations showed that 90° plies experienced early matrix tension failure in the bottom laminate and therefore were replaced with $\pm 15^\circ$ plies. The selected thickness of the buckling field laminate was 1.6 mm and 3.2 mm for the top laminate in the levers and the complete bottom laminate. The resulting laminate layups used in the finite element model and manufacturing were:

- Top laminate: $[90^\circ/-45^\circ/90^\circ/45^\circ/90^\circ/-45^\circ/90^\circ/45^\circ/0^\circ/45^\circ/0^\circ/-45^\circ/0^\circ/45^\circ/0^\circ/-45^\circ]_S$
- Buckling field laminate: $[90^\circ/-45^\circ/90^\circ/45^\circ/0^\circ/-45^\circ/0^\circ/45^\circ]_S$
- Bottom laminate: $[-45^\circ/45^\circ/-15^\circ/15^\circ/-45^\circ/45^\circ/0^\circ/-45^\circ/0^\circ/45^\circ/-15^\circ/15^\circ/0^\circ/-45^\circ/0^\circ/45^\circ]_S$

The analytical analysis required an approximation of the shear web because only symmetric laminates could be analysed. Further approximations were required for the choice of fibre tensile modulus in tension and compression, leading to the following layups:

- Top laminate: $[90^\circ/-45^\circ/90^\circ/45^\circ/90^\circ/-45^\circ/90^\circ/45^\circ/0^\circ/45^\circ/0^\circ/-45^\circ/0^\circ/45^\circ/0^\circ/-45^\circ]_S$,
with $E_{11c} = 130$ GPa and ply thickness 0.1 mm
- Buckling field laminate: $[90^\circ/-45^\circ/90^\circ/45^\circ/0^\circ/-45^\circ/0^\circ/45^\circ]_S$,
with $E_{11c} = 130$ GPa and ply thickness 0.1 mm
- Shear Web Laminate: $[-45^\circ/45^\circ/-15^\circ/15^\circ/-45^\circ/45^\circ/0^\circ/45^\circ/-15^\circ/15^\circ/0^\circ/-45^\circ]_S$,
with $E_{11c} = 130$ GPa and ply thickness 0.1 mm.
- Bottom Laminate: $[-45^\circ/45^\circ/-15^\circ/15^\circ/-45^\circ/45^\circ/0^\circ/-45^\circ/0^\circ/45^\circ/-15^\circ/15^\circ/0^\circ/-45^\circ/0^\circ/45^\circ]_S$,
with $E_{11t} = 160$ GPa and ply thickness 0.1 mm.

The prepreg was manufactured by North Thin Ply Technology with the material properties shown in Table 1.

Table 1. Prepreg properties for TP135/T800/100g

Prepreg Properties	Value	Unit
Ply Thickness	0.0953*	mm
Fibre Aerial Weight	100	g/m ²
Fibre Volume	60	%
Tensile Modulus E_{11T}	160*	GPa
Compression Modulus E_{11C}	130	GPa
Young's Modulus $E_{22,T=C}$	9.0*	GPa
Shear Modulus $G_{12} = G_{13}$	4.7	GPa
Shear Modulus G_{23}	4.7*	GPa
Poisson's Ratio ν_{12}	0.3*	-

* Data was estimated.

4. Experiment

The load-displacement curve was measured with a custom-built four-point bending jig on a universal Zwick tensile machine and a 100 kN load cell. The load introductions of the four-point bending jig were set 0.4 m apart, and the beam supports were set 0.375 m away from the load introductions (Fig. 5). The load introductions were steel loading pins with a 0.02 m diameter, fixed to the jig such that the pins could rotate around their axis. The beam supports were 0.06 m wide aluminium plates, pivoting around a steel pin. The test displacement speed was set to 10 mm/min. In order to evaluate possible influences of the displacement speed on the test results a test series was run. In the test series, the displacement speed was increased for every successive test up to 500 mm/min displacing the beam above the point of buckling. Despite different displacement speeds, no influences on the results were observed. The resulting bending moment M between the load introductions (Eq. (2)) is the product of the applied force F at one of the load introductions and the resulting distance between the load introduction and beam support (Fig. 5).

$$M = \frac{F}{2} \sqrt{Z_i^2 + 0.375^2} \quad (2)$$

The tensile machine measured the displacement between the load introductions and the beam supports Z . In the finite element analysis, only the nonlinear compliant section was simulated, therefore, only the beam midspan displacement ζ of the nonlinear compliant beam section relative to the load introductions is known. For comparing the experimental results with the simulation, the displacement results Z_i were converted by measuring Z and ζ at the maximum displacement in the experiment and scaling the displacement results Z_i accordingly to ζ_i (Eq. (3)).

$$\zeta_i = Z_i \cdot \zeta_{\max} / Z_{\max} \quad (3)$$

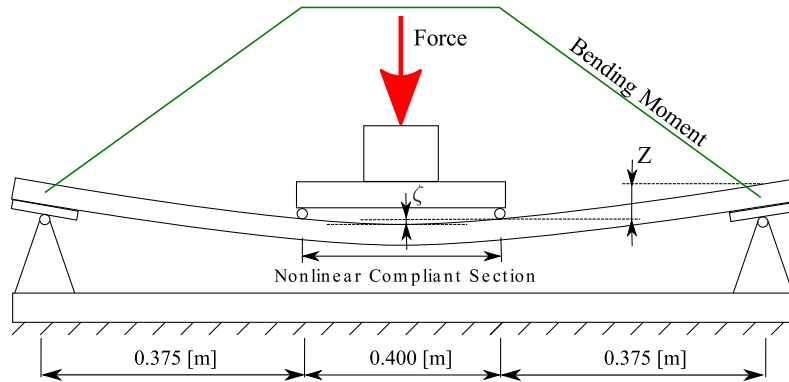


Figure 5. Dimensions and bending moment distribution of the four-point bending test.

5. Results and Discussion

The load-displacement curve of the experiment, the finite element model and the analytical model show very good agreement up to the point of buckling (Fig. 6).

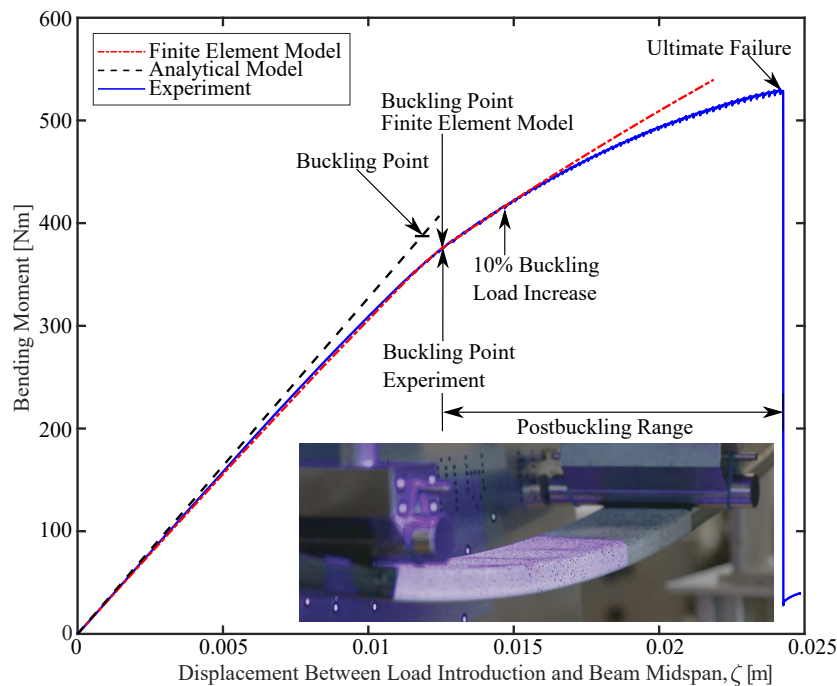


Figure 6. Analytical, numerical, and experimental load-displacement curves.

The analytical model does not capture the subsequent postbuckling state. In postbuckling, after a 10% buckling load increase the load-displacement curve of the finite element model and the experimental measurement start to deviate (Fig. 6 and 7). Note, the experimental data in postbuckling exhibits a saw-tooth noise in postbuckling as a result of the beam sliding on the supports in a stick-slip fashion while undergoing large deformation, and failing at 524 Nm. For further data processing the load-displacement curve of the finite element model and the experiment were approximated by cubic splines, which were then treated analytically.

Looking at the change in the bending stiffness of the finite element model and the experimental data (Fig. 7), which is the first derivative of the load-displacement curve, one may clearly observe the nonlinear compliance.

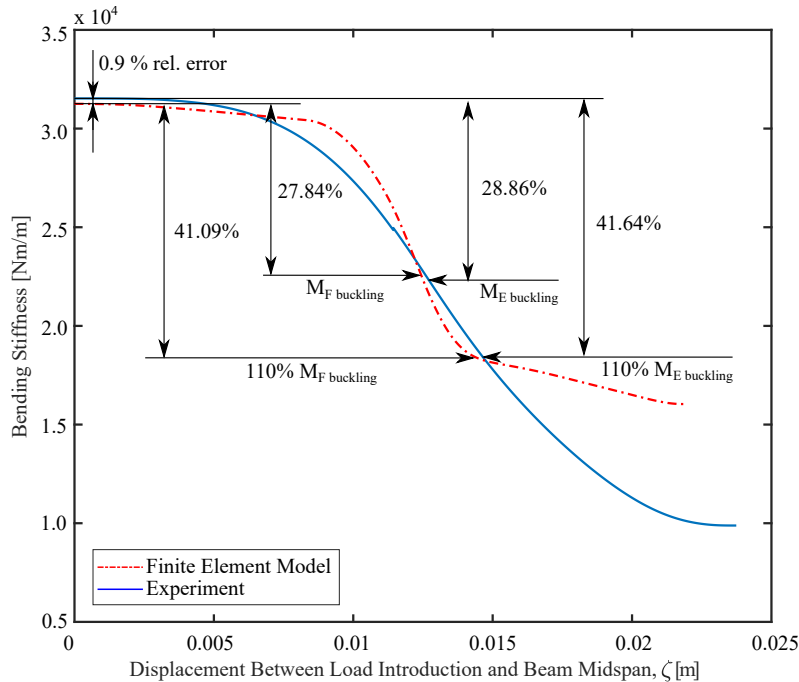


Figure 7. Change in beam bending stiffness with increasing beam displacement for the finite element model and the experiment.

The bending moment at the point of buckling M_{buckling} was determined by the point of inflection ($M''(\zeta) = 0$) in the bending stiffness plot (Fig. 7). For the experiment, $M_{E \text{ buckling}}$ is at 374.8 Nm, while $M_{F \text{ buckling}}$ is at 374.20 Nm for the finite element model, which results in a difference of 0.16% relative to the experiment. In comparison, the analytically derived $M_{A \text{ buckling}}$ is at 386.50 Nm, which yields an error of 3.1%, relative to the experiment. The analytically and numerically determined M_{buckling} agree very well with the experiment in spite of several simplifications. These very good agreements of M_{buckling} give confidence that compression flange buckling can be precisely tailored to a desired buckling load.

The initial bending stiffness showed a very high agreement between the finite element model and the experiment, with an error of 0.9% relative to the experiment. The error between the analytically derived and simulated initial bending stiffness is 3.8%, relative to the experiment. Leading up to the point of buckling the bending stiffness is reduced by 27.84% in the finite element model and by 28.86% in the experiment. At 110% M_{buckling} the initial bending stiffness is reduced by 41.09% in the finite element model and by 41.64% in the experiment. A reduction of 41.64% and more shows the effectiveness of compression flange buckling to achieve a nonlinear bending compliance, thereby providing the validity of the structural concept.

6. Conclusion

In this work a spanwise nonlinear compliance was, for the first time, achieved in carbon fibre reinforced polymer beams at high loads using local buckling in the compression flange. This structural concept may be used for passive spanwise bending shape adaption in wing-like structures and would enable a

wing to change its shape from a straight geometry into a strongly bent geometry without the need for actuators. Such change in geometry may be implemented to increase efficiency and manoeuvrability on vehicles with wing-like structures. This structural concept was proven analytically and numerically on a four-point bending beam and validated in an experiment. The results show a very high agreement with errors below 5% relative to the experiment. A bending stiffness reduction of 41.64% and more due to local flange buckling shows the effectiveness of the structural concept for nonlinear bending compliance.

Acknowledgments

The authors gratefully acknowledge the funding by the Swiss Innovation Agency - Innoswiss (Grant No. 19038.1 PFIW-IW - EHYCOMP).

References

- [1] L. F. Campanile. Being lightweight: a crucial requirement. In *Adaptive Structures: Engineering Applications*, D. Wagg, I. Bond, P. Weaver, and M. Friswell, Eds., Chichester: John Wiley & Sons, Ltd., 2007, chapter 4.4, pp. 95–104.
- [2] S. Barbarino, O. Bilgen, R. M. Ajaj, M. I. Friswell, and D. J. Inman. A Review of Morphing Aircraft. *Journal of Intelligent Material Systems and Structures*, 22(9):823–877, 2011.
- [3] J. Manzo and E. Garcia. Demonstration of an in situ morphing hyperelliptical cambered span wing mechanism. *Smart Materials and Structures*, 19(2):1–11, 2010.
- [4] S. R. Swanson. Analysis of Laminated Beams. In *Introduction to Design and Analysis with Advanced Composite Materials*, New Jersey: Prentice Hall Engineering/Science/Mathematics, 1997, chapter 7, pp. 191–223
- [5] L. P. Kollar and G. S. Springer. *Mechanics of Composite Structures*. Cambridge: Cambridge University Press, 2003.
- [6] R. M. Jones. *Mechanics of composite materials*. Philadelphia: Taylor & Francis, Inc., 2 edition, 1999.
- [7] *Abaqus/CAE 6.13-1*. Dassault Systèmes Simulia Corp., Providence, Rhode Island, USA, 2013.